East Asian methane emissions inferred from high-resolution inversions of GOSAT and TROPOMI observations: a comparative and evaluative analysis

Ruosi Liang[1,2,3], Yuzhong Zhang[2,3], Wei Chen[1,2,3], Peixuan Zhang[2,3,4], Jingran Liu[1,2,3], Cuihong Chen[5], Huiqin Mao[5], Guofeng Shen[6], Zhen Qu[7], Zichong Chen[8], Minqiang Zhou[9], Pucai Wang[9,10], Robert J. Parker[11,12], Hartmut Boesch[11,12], Alba Lorente[13], Joannes D. Maasakkers[13], Ilse Aben[13]

[1]Zhejiang University, Hangzhou, Zhejiang 310027, China

[2]Key Laboratory of Coastal Environment and Resources of Zhejiang Province, School of Engineering, Westlake University, Hangzhou, Zhejiang 310030, China

[3]Institute of Advanced Technology, Westlake Institute for Advanced Study, Hangzhou, Zhejiang 310024, China

[4]Fudan University, Shanghai 200433, China

[5]Center for Satellite Application on Ecology and Environment, Ministry of Ecology and Environment of China, Beijing 100094, China

[6]Laboratory for Earth Surface Processes, College of Urban and Environmental Sciences, Peking University, Beijing 100871, China

[7]Department of Marine Earth and Atmospheric Sciences, North Carolina State University, Raleigh, NC 27607, USA

[8]School of Engineering and Applied Science, Harvard University, Cambridge, MA, USA

[9]Institute of Atmospheric Physics, Chinese Academy of Sciences, Beijing 100029, China

[10]University of Chinese Academy of Sciences, Beijing 100049, China

[11]National Centre for Earth Observation, University of Leicester, Leicester, UK

[12]Earth Observation Science, School of Physics and Astronomy, University of Leicester, Leicester, UK

[13]SRON Netherlands Institute for Space Research, Utrecht, Netherlands

Correspondence to: Yuzhong Zhang (zhangyuzhong@westlake.edu.cn)

Abstract. We apply atmospheric methane column retrievals from two different satellite instruments (GOSAT and TROPOMI) to a regional inversion framework to quantify East Asian methane emissions for 2019 at $0.5° \times 0.625°$ horizontal resolution. The goal is to assess if GOSAT (relatively mature but sparse) and TROPOMI (new and dense) observations inform consistent methane emissions from East Asia with identically configured inversions. Comparison of the results from the two inversions show similar correction patterns to the prior inventory in Central North China, Central South China, Northeast China, and Bangladesh, with less than 2.7 Tg a^{-1} differences in regional posterior emissions. The two inversions, however, disagree over some important regions particularly in northern India and East China. The inferred methane emissions by GOSAT observations are 7.7 Tg a^{-1} higher than those by TROPOMI observations over northern India but 7.0 Tg a^{-1} lower over East China. We find that the lower methane emissions from East China inferred by the GOSAT inversion are more consistent with independent ground-based *in situ* and total column (TCCON) observations, indicating that the TROPOMI retrievals may have high XCH$_4$ biases in this region. We also evaluate inversion results against tropospheric aircraft observations over India during 2012-2014 by using a consistent GOSAT inversion of earlier years as an inter-comparison platform. This indirect evaluation favors lower

methane emissions from northern India inferred by the TROPOMI inversion. We find that in this case the discrepancy in emission inference is contributed by differences in data coverage (highly uneven observations by GOSAT vs. good spatial coverage by TROPOMI) over northern India.

1 Introduction

40   Methane (CH_4) is a powerful greenhouse gas, with a global warming potential ~80 times that of carbon dioxide (CO_2) on a 20-year timescale and ~30 times on a 100-year timescale (Forster et al., 2021). In 2020, the atmospheric methane concentration has increased to 1889±2 ppbv, 262% of pre-industrial levels in 1750, driven primarily by increasing anthropogenic emissions (WMO, 2021). The last decade has seen a rapid growth of atmospheric methane (~ 8.6 ppbv a^{-1}), after a brief period of stabilization in the early 2000s (Dlugokencky et al., 2011; Fletcher and Schaefer, 2019; Rigby et al., 2008; Yin et al., 2021;

45   Zhang et al., 2021). Rising methane concentrations, if continued at current rates in coming decades, may negate benefits of CO_2 emission reduction and therefore curbing methane emissions in the 2020s is vital for the success of the Paris Agreement (Ganesan et al., 2019; Nisbet et al., 2019).

Information on methane emissions is required at global, national, and regional levels to guide climate actions on methane.

50   Current bottom-up inventories are often inadequate for this purpose because of their large uncertainties in emission factors and lack of information on emission activities (Saunois et al., 2020). Independent measurements of atmospheric methane, including those from satellite remote sensing, are thus used to evaluate and improve these bottom-up inventories (Jacob et al., 2016). This is generally done through an inversion of atmospheric observations with a chemical transport model to characterize the relationship between emissions and concentrations. Atmospheric methane is measured by two classes of satellite instruments,

55   point source imagers and area flux mappers. While point sources imagers (e.g., Sentinel-2, Landsat, GHGSat) specialize in detecting large emissions from point sources, area flux mappers provide high-precision measurements that can be used to constrain methane fluxes on regional and global scales (Jacob et al., 2022). Area flux mappers that are currently in operation include the TANSO-FTS instrument onboard the Greenhouse gases Observing SATellite (GOSAT) launched in 2009 (Kuze et al., 2016) and the more recent TROPOspheric Monitoring Instrument (TROPOMI) onboard the Sentinel 5 Precursor (S5P)

60   satellite launched in 2017 (Hu et al., 2016; Lorente et al., 2021; Veefkind et al., 2012). Satellite observations made by these area flux mappers are especially valuable in constraining methane emissions over regions with no or only sparse ground networks, including Africa, South America, and East and South Asia (Lu et al., 2021).

Both GOSAT and TROPOMI operate in sun-synchronous orbits and retrieve column-averaged dry-air methane mole fractions

65   (XCH_4) from backscattered solar shortwave infrared radiation. TROPOMI continuously images the land surface at a pixel resolution of 7 km × 7 km (5.5 km × 7 km after August 2019) with daily global coverage (Hu et al., 2018; Lorente et al., 2021; Sha et al., 2021), while GOSAT in its standard-viewing mode measures with a 3 day return time in 10 km diameter circular

footprints that are typically spaced ~250 km apart (Butz et al., 2011; Kuze et al., 2009; Kuze et al., 2016; Yokota et al., 2009). As a result of differing sampling strategies, TROPOMI generates much higher observation density than GOSAT, which in

70   principle should benefit fine-resolution inversions. The two instruments also measure at different wavelengths, GOSAT at the 1.65 μm band and TROPOMI at the 2.3 μm band. This affects the algorithm that can be applied to retrieve XCH_4. Operational TROPOMI retrievals use the RemoTeC full-physics method (Hu et al., 2018). The method is prone to spatially and temporally variable biases owing to scattering artefacts (Hu et al., 2018; Lorente et al., 2021; Sha et al., 2021). These biases in general are not reducible with more observations and, if not corrected, can translate into biases in emission estimates in an inversion.

75   Because of spectrally adjacent CO_2 and CH_4 absorption in the 1.65 μm band, GOSAT retrievals can alternatively use the CO_2 proxy method, in which XCH_4 is derived from directly retrieved CH_4 to CO_2 column ratios and independently specified (simulated or assimilated) CO_2 columns (Alexe et al., 2015; Frankenberg et al., 2005; Frankenberg et al., 2006; Parker et al., 2015; Parker et al., 2020). The proxy method usually results in reduced variable biases, as scattering artefacts largely cancel out in retrieving CH_4 to CO_2 column ratios. It is, however, subject to any errors in specified CO_2 columns. The proxy method

80   also leads to a better retrieval success rate over regions with high aerosol loadings or thin clouds, as the method is less sensitive to these interferences compared to the full-physics approach.

A number of studies have applied GOSAT data in inversions on a range of scales (Cressot et al., 2014; Feng et al., 2022; Lu et al., 2021; Maasakkers et al., 2019; Monteil et al., 2013; Pandey et al., 2016; Turner et al., 2015; Zhang et al., 2021).

85   TROPOMI data have also been applied in several regional inversion studies (Chen et al., 2022; McNorton et al., 2022; Shen et al., 2021; Shen et al., 2022; Zhang et al., 2020) often with the focus on resolving fine-scale emission hotspots. Qu et al. (2021) performed global inversions of GOSAT and TROPOMI observations at 2° × 2.5° resolution in a comparative analysis, and they showed that methane emissions inferred from the two inversions are generally consistent on the global scale but with significant regional discrepancies including over China.

90

Here we present high-resolution (0.5° × 0.625°) inversions of GOSAT and TROPOMI observations over East Asia. The main objective is to assess the consistency of methane fluxes inferred from the two sets of satellite data that differ in their data coverage and regional accuracy, adding information to the uncertainty characterization of satellite-based methane emission accounting. We perform the analyses with identically configured inversions to isolate the effects of observation data, and we

95   further use independent ground-based observations to evaluate the discrepancies between the two inversions and discuss the cause of differences. This study focuses on East Asia (including China and northern India), which is one of the world's major methane emitting regions and accounts for more than 20% of global emissions (UNFCCC, 2020). The region has been an important contributor to global increases in methane emissions, but the magnitude of the trend and its sectoral attributions are debated (Ganesan et al., 2017; Gao et al., 2021; Liu et al., 2021; Miller et al., 2019; Sheng et al., 2021; Zhang et al., 2021).

2 Observation Data

2.1 Satellite observations

We used XCH$_4$ observations from GOSAT and TROPOMI for 2019 in regional inversions over East Asia. For GOSAT, we use the University of Leicester Proxy XCH4 v9.0 retrievals (Parker and Boesch, 2020). This product is based on the CO$_2$ proxy method, which, as described above, limits variable biases associated with scattering artefacts but is subject to any biases in specified CO$_2$ columns (Parker et al., 2015). We use in our inversion only high-quality GOSAT retrievals flagged as "xch4_quality_flag=0" over both land and ocean (glint mode).

For TROPOMI, we use the SRON RemoTeC-S5P XCH$_4$ scientific product, from Lorente et al. (2021). The improved algorithm by Lorente et al. (2021) was later implemented in the official operational product (v2.02.00) in July 2021 (Lorente et al., 2022). They derived an empirical correction formula to improve surface reflectance dependent biases identified in TROPOMI full-physics retrievals. The correction significantly improves data quality over scenes with low (e.g. snow cover) and high surface albedo (e.g. deserts) which are challenging for a full-physics algorithm. Large corrections are made in East China, Xinjiang China, Southeast Asia, and Siberia (Figure S1). Bias-corrected TROPOMI retrievals flagged with "qa_value = 1" are used for inversion. This version of the TROPOMI product does not provide ocean glint-mode retrievals.

Figure 1 shows the spatial distributions of annual average XCH$_4$ on the 0.625° × 0.5° grid for GOSAT and TROPOMI. Both datasets show high XCH$_4$ in eastern China and northern India and low XCH$_4$ over Mongolian and Tibetan plateaus, although TROPOMI provides much better spatial coverage than GOSAT over most regions. There are in total 45,018 observations for GOSAT and 8,860,722 for TROPOMI. We take averages of multiple measurements fall in a 0.625° × 0.5° grid cell on any individual day (this procedure affects primarily dense TROPOMI data), and the resulting gridded daily observations are used in the inversion. The spatial distribution of gridded daily observation numbers is shown in Figure S2.

We refer to the XCH$_4$ retrieval products used in this study as GOSAT or TROPOMI observations and corresponding inversions as GOSAT or TROPOMI inversions for simplicity. There are other operational and scientific retrieval products available from both GOSAT and TROPOMI measurements (e.g., the operational GOSAT XCH$_4$ retrieval (Yoshida et al., 2013), the scientific TROPOMI/WFMD XCH$_4$ retrieval (Schneising et al., 2019)). Our analyses and conclusions are specific to the two retrieval products used here, though we expect that some of them can also apply to other retrievals.
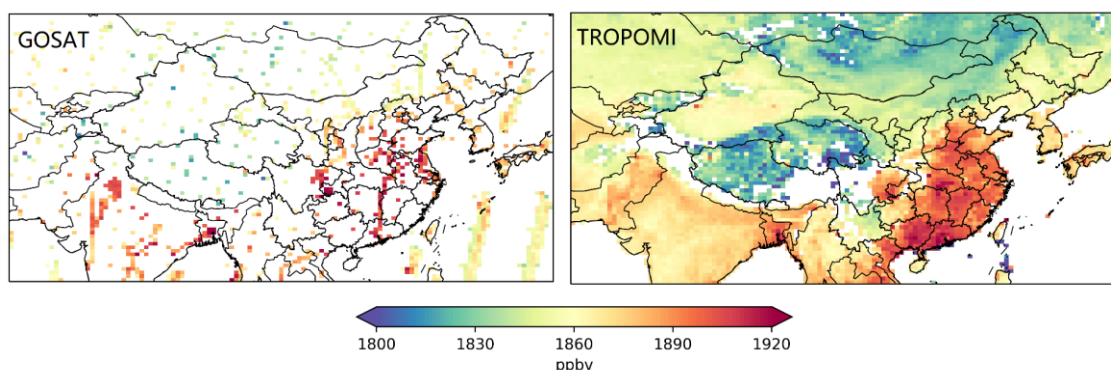
Figure 1: 2019 annual average methane column mole fractions over the East Asia domain for GOSAT (UoL proxy v9.0 retrieval) and TROPOMI (Lorente et al. (2021) full-physics retrieval), presented on the 0.5° × 0.625° GEOS-Chem grid.

2.2 Independent evaluation data

We use a suite of independent high-quality methane observations to evaluate the posterior emissions inferred from satellite observations, including surface *in situ* observations, ground-based remote sensing observations, and tropospheric *in situ* measurements from commercial airlines. Table S1 provides a descriptive list of these surface sites and Figure 2 shows the locations of surface sites and a representative flight path. These suborbital observations are of good accuracy and precision compared to satellite observations.

Surface *in situ* observations are available through World Data Centre for Greenhouse Gases (WDCGG) or the CH_4 GLOBALVIEWplus v4.0 ObsPack (Schuldt et al., 2021). The five sites are Anmyeon-do, South Korea (AMY), Pha Din, Vietnam (PDI), Lulin, Taiwan China (LLN), Ulaan Uul, Mongolia (UUM), Waliguan, China (WLG) (Dlugokencky et al., 1994; Dlugokencky et al., 2021; Lee et al., 2019; Nguyen Nhat Anh and Steinbacher, 2021). Observations are done with either continuous (hourly) online instruments or weekly collected flask (Table S1). Most of these sites are continental or subcontinental background sites (PDI, LLN, UUM, and WLG), and their observations are insensitive to local methane emissions. An exception is AMY which is affected by local Korean emissions as well as upwind East China emissions.

Total methane column observations by ground-based Fourier Transform Spectrometers are available at two TCCON sites located in East China, Hefei, China (HF) and Xianghe, China (XH) (Liu et al., 2022; Yang et al., 2020), and their observations are sensitive to methane emissions from East China. We note that a previous evaluation of GOSAT and TROPOMI against TCCON did not include data from these two sites, as their data were not available then (Qu et al., 2021). We use only measurements with solar zenith angles < 60° to ensure high data quality.

All the above surface sites are located distant from northern India, which is a major methane emitting region in the study domain. The only relevant dataset available to us in this area comes from the Civil Aircraft for the Regular Investigation of the atmosphere Based on an Instrument Container (CARIBIC) project (available via the CH4 GLOBALVIEWplus v4.0 ObsPack (Schuldt et al., 2021)), which includes regular flights in the troposphere over northern India. However, these data are collected in earlier years between 2012 and 2014 before the time of TROPOMI. In the absence of better observation data, we compare these 2012-2014 aircraft observations to a simulation driven by a similarly configured GOSAT inversion for an earlier period (2010-2017) (Zhang et al., 2022). By doing so, we assume that any systematic bias derived from this comparison should still be representative of the 2019 GOSAT inversion.
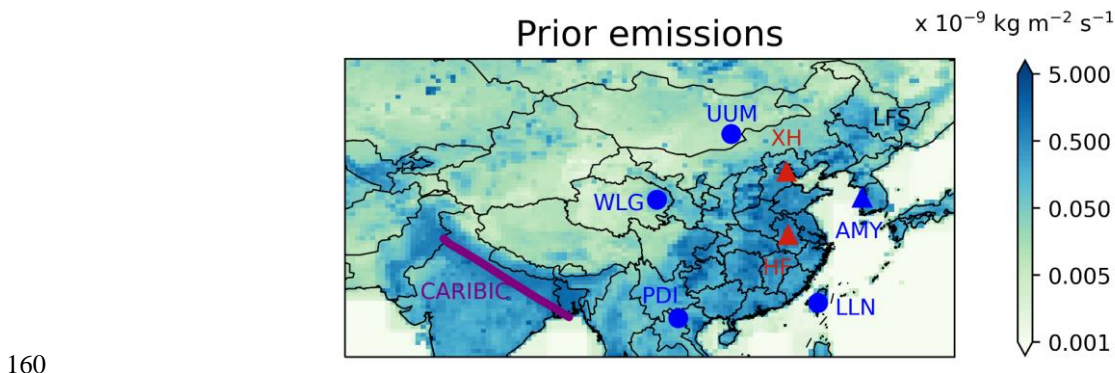
Figure 2: Spatial distribution of prior emissions. Locations of independent data for evaluation (seven surface sites and aircraft route) are shown. Circles represent background sites and triangles source-region sites. Total column measurements are coded in red and *in situ* measurements in blue. Purple solid line shows a CARIBIC aircraft route that measured tropospheric methane over India on November 22, 2012.

3 Inverse analysis

3.1 Forward model and prior emissions

We use GEOS-Chem v12.9.3 as the forward model for the inversion. The simulation is conducted for 2019 over East Asia (15°N-55°N, 60°E-140°E) on a 0.5° × 0.625° horizontal grid with 47 vertical layers and is driven by MERRA-2 meteorological fields from the NASA Global Modeling and Assimilation Office (GMAO) (Gelaro et al., 2017). The initial concentration fields on January, 1, 2019 and 3-hourly boundary conditions for the nested domain are taken from a global inversion of TROPOMI data for 2019 (Qu et al., 2021). We find that the boundary conditions from this global inversion still have biases over East Asia (more discussion in Section 4.3.3), which may partly be due to the fact that Qu et al. (2021) used an early version of TROPOMI retrievals. In our inversion, we optimize for systematic biases at four lateral boundaries together with methane emissions.

Prior emissions (Figure 2) used in GEOS-Chem simulations are compiled from bottom-up sectoral inventories (Table S2). In brief, we use EDGAR v4.3.2 (Janssen-Maenhout et al., 2019) for anthropogenic methane emissions, with those from fossil

fuel exploitation replaced by Scarpelli et al. (2020) (oil and gas; coal outside of China) and Sheng et al. (2019) (coal in China). A comparison with a more recent inventory EDGAR v6 shows no large revisions of anthropogenic methane emissions over the study region that we expect to have a great impact on the inversion results (Figure S3). For natural emissions, we use the WetCHARTs version 1.0 inventory for wetlands (Bloom et al., 2017), the Quick Fire Emissions Dataset (QFED) v2.4r8 for biomass burning, Fung et al. (1991) for termite emissions, and Maasakkers et al. (2019) for geological sources.

While methane sinks are not optimized in our regional inversion, they are explicitly simulated in GEOS-Chem simulations. We use monthly OH fields from a full-chemistry GEOS-Chem simulation (Wecht et al., 2014) and soil absorption from Murguia-Flores et al. (2018).

3.2 Inversion procedure

We perform analytical Bayesian inversions to optimize a state vector x containing annual methane emissions from 600 clusters and average methane column biases at four model boundaries. We optimize emissions on 600 spatial clusters instead of the native $0.5° \times 0.625°$ grid, which are generated based on a Gaussian Mixed Model (GMM) algorithm proposed by Turner and Jacob (2015). This strategy significantly reduces the computation of an analytical inversion while accounting for major patterns in the distribution of methane emissions. We also optimize for biases in boundary conditions on four sides of our domain (east, south, west, north). Examination of our prior simulation finds domain-wide biases against either GOSAT or TROPOMI observations that can only be attributed to biased boundary condition.

Assuming a Gaussian distribution of error, the optimal estimate of x is obtained by minimizing the cost function (Brasseur and Jacob, 2017; Rodgers, 2000):

$$J(x) = (x - x_A)^T S_A^{-1}(x - x_A) + \gamma(y - F(x)) S_O^{-1}(y - F(x)) \tag{1}$$

where x_A is prior estimates for x and y is the observation vector containing either TROPOMI or GOSAT observations, and F is a function of x representing the forward model. S_A and S_O are respectively prior and observation error covariance matrices. We take S_A as a diagonal matrix and assume a 50% standard deviation for prior emissions and a 1% standard deviation for boundary conditions. S_O is also taken as diagonal and is populated following the residual error method (Heald et al., 2004), which finds that observation error standard deviations average 16 ppbv for TROPOMI and 18 ppbv for GOSAT. γ is a regularization parameter to balance prior and observation information (Hansen, 1998; Rodgers, 2000) and is introduced to prevent overfitting from omitting error correlations in S_O. The degree of spatial error correlations varies substantially from GOSAT to TROPOMI observations because of their differences in data densities; therefore, we expect different γ values to be taken for the two datasets. We determine γ following Lu et al. (2021) and Qu et al. (2021), and find $\gamma = 0.09$ for TROPOMI and $\gamma = 0.6$ for GOSAT (Figure S4). A smaller γ for TROPOMI reflects a higher degree of spatial correlation among denser TROPOMI observations.

The forward model (GEOS-Chem) can be described by a linear equation:

$$F(x) = Kx, \tag{2}$$

where $K = \nabla_x F$ is the Jacobian matrix, which describes the sensitivity of observations to the state vector. The cost function is minimized at $\nabla_x J(x) = 0$, which yields the optimal estimate ($\hat{x}$)

$$\hat{x} = x_A + (\gamma K^T S_0^{-1} K + S_A^{-1})^{-1} \gamma K^T S_0^{-1} (y - Kx_A), \tag{3}$$

with the posterior error covariance matrix $\hat{S}$

$$\hat{S} = (\gamma K^T S_0^{-1} K + S_A^{-1})^{-1} \tag{4}$$

and the averaging kernel matrix A that describes the sensitivity of the optimal solution to the true value:

$$A = \frac{\partial \hat{x}}{\partial x} = I_n - \hat{S} S_A^{-1}. \tag{5}$$

The trace of A is referred to as the degree of freedom for signals (DOFS), which represents the number of independent pieces of information constrained by an observing system.

4 Results and discussion

4.1 Comparison of methane emissions from TROPOMI and GOSAT inversions

Figure 3 shows the correction patterns of methane emissions (posterior - prior emissions) inferred respectively from TROPOMI and GOSAT inversions. Both inversions find that the prior inventory underestimates methane emissions from Northeast China (NEC) and Bangladesh (BAN) and overestimate emissions from Central South China (CSC). The two inversions also find similar correction patterns in Central North China (CNC) with upward adjustments over central Shanxi and downward adjustments over neighboring Henan province. These agreements reflect some consistencies between TROPOMI and GOSAT inversions at the regional level.

TROPOMI and GOSAT inversions show large differences over important source regions, including East China (EC) and northern India (IND) (Figure 3). While the GOSAT inversion suggests that methane emissions over IND should be increased and those from EC decreased relative to prior estimates, the TROPOMI inversion finds the opposite. As a result, regional total methane emissions inferred by the two inversions differ by 7.7 Tg a^{-1} or 27% over IND (TROPOMI: 24.7$\pm$0.6 Tg a^{-1}, GOSAT: 32.4$\pm$0.7 Tg a^{-1}) (errors reported for regional estimates are 1σ standard deviations derived from posterior error covariance matrices) and by 7.0 Tg a^{-1} or 32% over EC (TROPOMI: 28.3$\pm$0.9 Tg a^{-1}, GOSAT: 21.3$\pm$0.9 Tg a^{-1}) (Figure 3c). In addition, the two inversions also disagree over the northwestern part of the domain (NWD including parts of Kazakhstan and northern Xinjiang, China and SXJC including mainly southern Xinjiang, China), where TROPOMI indicates large upward adjustments while GOSAT finds agreement with the prior inventory.
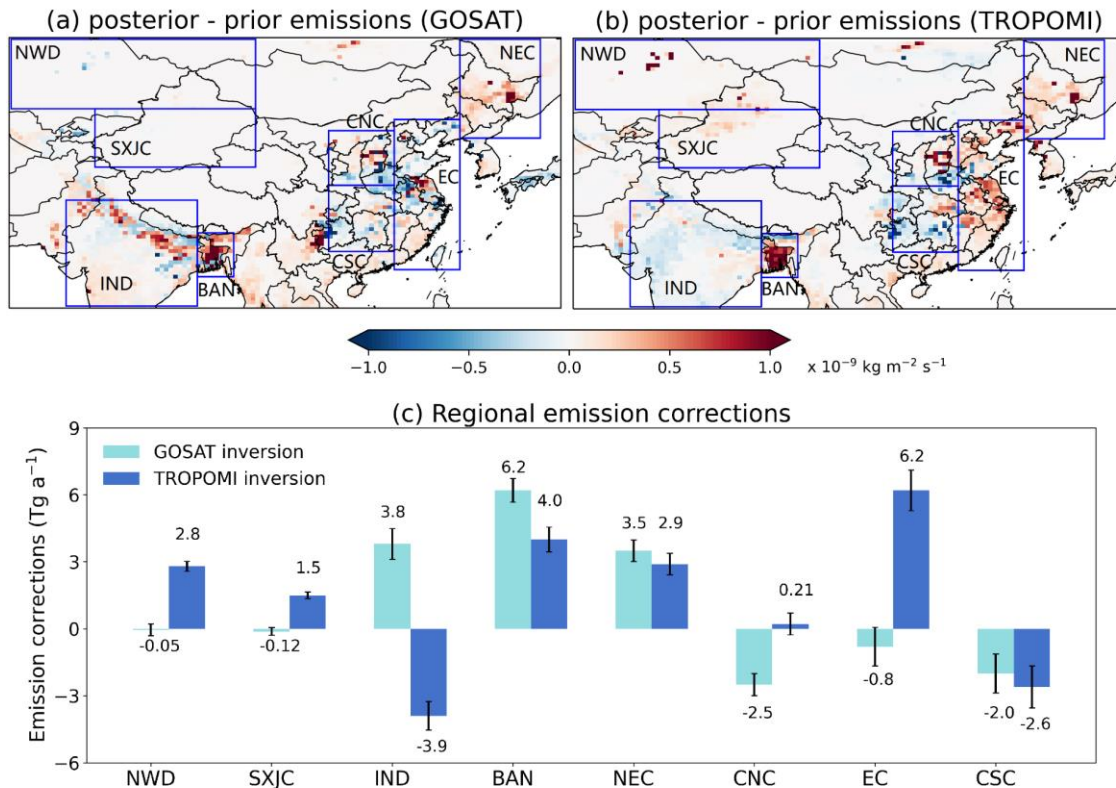
Figure 3: Spatial distributions of methane emission corrections (posterior - prior) inferred by (a) GOSAT and (b) TROPOMI inversions. (c) shows emissions aggregated by region as defined in blue rectangles in (a) and (b). Error bars represent the standard deviation of regional estimates derived from posterior error covariance matrices. These errors do not include systematic uncertainties due to inversion setups and are thus optimistic, but they are relevant for comparing results from two identically configured inversions.

We perform sensitivity inversions to examine the impact of inversion configurations (i.e., optimizing emissions seasonally instead of annually, increasing prior error of methane emissions to 100%) on the above comparison of TROPOMI and GOSAT inversions. We find that the major findings of the comparison (agreement in NEC, BAN, and CSC; disagreement in EC, IND, NWD, SXJC) (Figure 3) are robust against these perturbations (Figure S5 and Figure S6), as the effects of inversion configurations are mainly systematic and therefore similar for both inversions.

Table S2 summarizes methane emission estimates from TROPOMI and GOSAT inversions over the entire East Asia domain and over China. The two inversions find similar posterior methane emissions from East Asia (TROPOMI: 143.5 ± 1.4 Tg a^{-1}; GOSAT: 146.2 ± 1.2 Tg a^{-1}), with differences in China (TROPOMI: 74.9 ± 1.0 Tg a^{-1}; GOSAT: 68.1 ± 1.0 Tg a^{-1}) largely canceled out by differences in northern India. For China, we attribute 69.1 Tg a^{-1} for the TROPOMI inversion and 63 Tg a^{-1} for the GOSAT inversion to anthropogenic emissions, based on prior sectoral fractions in each spatial cluster. These values

are at the high end of previous inversion-based estimates of 43-62 Tg a^{-1} (Deng et al., 2022; Lu et al., 2021; Miller et al., 2019; Qu et al., 2021; Saunois et al., 2020; Sheng et al., 2021; Stavert et al., 2022; Wang et al., 2021; Zhang et al., 2021; Zhang et al., 2022) and are higher than China's latest submission to the UNFCCC (55 Tg a^{-1}) for 2014 (UNFCCC, 2020). These previous inversions mainly used GOSAT observations but differ greatly in their inversion setups (e.g., time, domain coverage, spatial resolution, transport model), thus resulting in a considerable range of estimates. In contrast, the differences in inversions presented in this work are fully due to satellite observations. Our TROPOMI inversion results are consistent with a recent TROPOMI inversion study by Chen et al. (2022) who reported estimate of China's total, anthropogenic, and natural methane emissions of 70.0 (61.6-79.9), 65.0 (57.7-68.4), and 5.0 (3.9-11.6) Tg a^{-1}.

4.2 Evaluation of inversion results with independent observations

Both TROPOMI and GOSAT posterior simulations can reduce errors against their respective "training" data relative to the prior simulation (Figure 4), which is expected for successful inversions. However, concentration fields from the two simulations show varied degrees of agreement across the domain (Figure 5a). In this section, we use independent high-quality observations to evaluate whether GOSAT and TROPOMI inversion results are consistent, and in the case that they are not, which one is in better agreement with independent data.

Table 1 summarizes performance metrics against these independent observations. GOSAT and TROPOMI inversions perform similarly at background sites such as PDI, UUM, WLG, and LLN. Both posterior simulations considerably reduce biases against *in situ* observations at WLG and PDI and achieve relatively good agreement at PDI, UUM, and WLG (absolute biases < 7 ppbv and R^2 between 0.39-0.72). An exception is LLN (a high-mountain background site in the southeast of the domain) where biases grow larger in both posterior simulations (11.0 ppbv for GOSAT and 16.7 ppbv for TROPOMI). This is mainly caused by large seasonal biases in the eastern boundary (Figure 5c) (see Section 4.3.3 for more discussion). In fact, mean biases at LLN decrease from prior to posterior simulations during January to May of the year (Prior: -10.8 ppbv; GOSAT: 1.2 ppbv; TROPOMI: 3.7 ppbv) but increase for June to December (Prior: 7.5 ppbv; GOSAT: 17 ppbv; TROPOMI: 24.7 ppbv).

On the other hand, methane concentrations from the TROPOMI and GOSAT posterior simulations differ by ~10-20 ppbv at sites in methane source regions (i.e., XH and HF within EC and AMY in Korea downwind EC) (Figure 5a). Their differences in concentrations are due mainly to higher methane emissions inferred by the TROPOMI inversion than GOSAT over EC (by 7.0 Tg a^{-1}) and Korea (Figure 3). Our evaluation against in situ measurements at AMY and total column measurements at XH and HF shows consistently high biases of ~15-25 ppbv by the TROPOMI posterior simulation and a comparatively better agreement (bias ~8 ppbv) with the GOSAT posterior simulation (Table 1). Smaller mean biases are achieved by the prior simulation at XH and HF (Table 1), but this is largely because of the low background concentration caused by biases in prior boundary conditions (as indicated by the large negative prior bias at the upwind background site WLG; Table 1). Overall, our

results at AMY, XH, and HF supports the lower methane emissions from EC inferred by the GOSAT inversion over the TROPOMI inferences and indicates that TROPOMI XCH$_4$ retrievals may have regional high biases over EC (more discussion in 4.3.1).

295   Methane concentrations from the TROPOMI and GOSAT posterior simulations differ by 5.2 ppbv on average along the CARIBIC flight tracks over the Ganges Plain (Figure 5a). This difference is mainly due to different IND methane emissions between the two inversions (Figure 5b) with minor contributions from boundary condition bias inferences (Figure 5c). In the absence of concurrent independent observations over IND, we use CARIBIC aircraft observations that are only available from 2012 to 2014 to evaluate the inversions. Since these observations predate TROPOMI, we can only indirectly evaluate by using
300   a simulation driven by methane emissions from a GOSAT inversion for earlier years as an inter-comparison platform. We take inversion results from a previous study (Zhang et al., 2022), which performed an East Asia inversion also using GOSAT proxy XCH$_4$ retrievals. Their inversion is almost identically configured as this study except that it was for 2010-2017. Consistent with our GOSAT results, the GOSAT inversion from Zhang et al. (2022) also found that IND methane emissions should be adjusted upward.
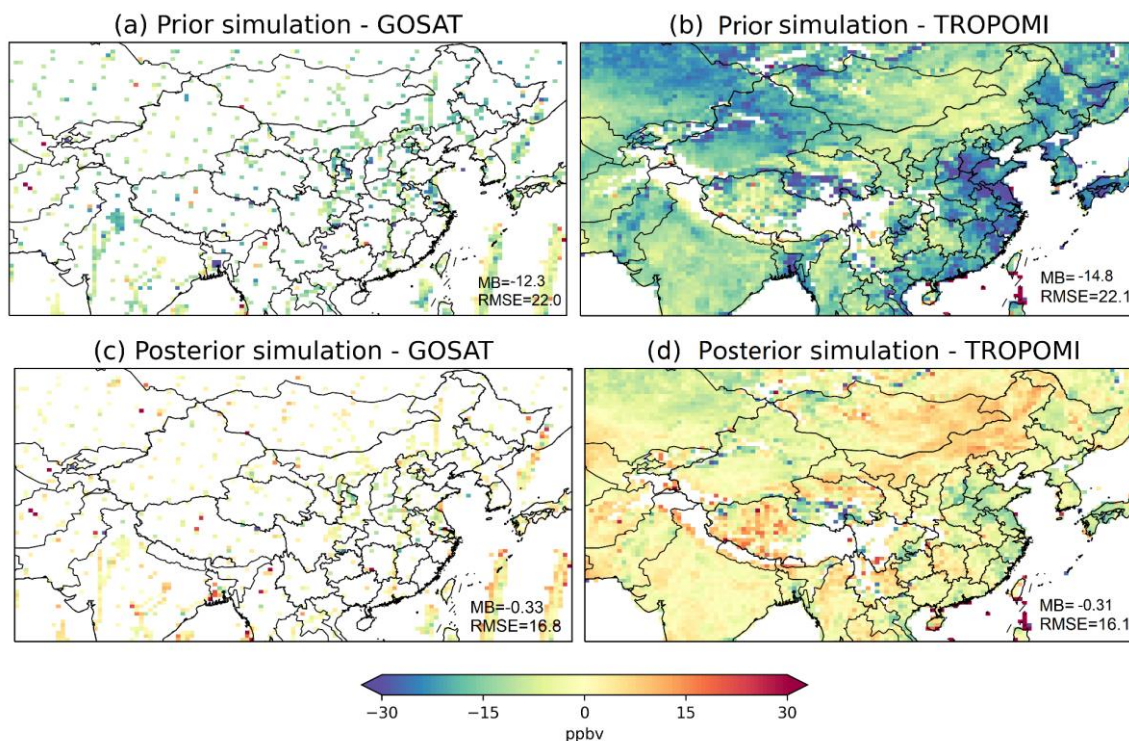
305

Figure 4: Differences in XCH$_4$ between simulations and satellite observations from GOSAT (a and c) and TROPOMI (b and d). (a) and (b) show results for the prior simulation, (c) for the posterior simulation driven by the GOSAT inversion, and (d) for the posterior simulation driven by the TROPOM inversion. Root-mean-square errors (RMSE, in ppbv) and mean biases (MB, in ppbv, simulation - observation) are inset.

310

Table 1: Evaluation of simulated methane concentrations against independent observations[a].

Site	Mean Bias±Standard Error (ppbv)			$R^{2\,b}$		
	Prior	GOSAT	TROPOMI	Prior	GOSAT	TROPOMI
AMY	-5.9±2.5	7.5±2.4	25.5±2.4	0.46	0.5	0.46
PDI	-20±2.3	-3.7±2.2	-1.3±2.3	0.67	0.7	0.69
LLN	0.5±4.1	11.0±4.3	16.7±4.3	0.39	0.4	0.37
UUM	-9.0±2.1	5.8±2.1	6.6±2.2	0.71	0.71	0.72
WLG	-16.6±2.7	-4.3±2.9	-2.7±2.7	0.4	0.39	0.41
XH[c]	-3.4±1.0	7.9±0.9	15.2±1.0	0.72	0.74	0.73
HF[c,d]	1.0±3.0	8.0±3.0	20.8±3.0	0.5	0.51	0.55
CARIBIC[e]	-	14.9±0.8	9.7±0.8	-	-	-

[a] Five sites report surface *in situ* measurements with PDI, LLN, UUM, and WLG being continental-scale background sites and AMY a regional site. Two sites (XH and HF) located in East China report ground-based total column measurements. The aircraft measurements (CARIBIC) are taken over northern India.

315 [b] Inversions are unable to improve performance for temporal variability. This is limited by the fact that optimization of methane emissions is done only annually. Other factors include model transport errors and observation representativeness.

[c] Small prior biases at XH and HF should not be interpreted as evidence for unbiased prior emissions from EC, because the prior simulation has substantial low biases in background concentrations as shown by data at WLG (upwind of EC).

[d] Large biases between simulations and observations occur in five days (Jul. 22rd, Sept. 30th, Nov. 3rd, Nov. 23rd and Dec. 3rd) at site HF.
320 Relatively low R^2 in this line are largely affected by these data. Excluding this subset of observations results in correlation coefficients of ~0.8 for all simulations and mean biases of -2.9±1.4, 4.4±1.3, and 17.6±1.7 ppbv for prior, GOSAT, and TROPOMI simulations, respectively.

[e] Indirect evaluation is performed for CARIBIC data. The value in the 'GOSAT' column represents the mean bias between the posterior simulation of the 2010-2017 GOSAT inversion and 2012-2014 CARIBIC aircraft observations. We assume that GOSAT inversions are
325 consistent between years so that the 2012-2014 bias is representative for the 2019 condition. The value in the 'TROPOMI' column is computed by subtracting the mean difference along aircraft paths between 2019 GOSAT and TROPOMI posterior simulations (~5.2 ppbv) (Figure 5a) from the 2012-2014 GOSAT bias. R^2 is not reported for this indirect comparison.

Comparison with these aircraft observations indicates that the 2012-2014 simulation driven by GOSAT-optimized emissions
330 from Zhang et al. (2022) overestimates the aircraft observations by ~14.9 ppbv (Table 1). On the other hand, the 2019 posterior simulation from the GOSAT inversion is about 5.2 ppbv higher than that from the TROPOMI inversion along flight tracks (Figure 5a). Assuming that our 2019 GOSAT inversion is consistent with the 2010-2017 GOSAT inversion by Zhang et al. (2022) (mean bias 14.9 ppbv), it thus suggests that the TROPOMI inversion likely agrees better with the CARIBIC

observations (mean bias 9.7 ppbv) than the GOSAT inversion. Unlike the EC case, we find over IND relatively small systematic differences in TROPOMI and GOSAT XCH$_4$ retrievals (Figure 6). Our analysis suggests that good data coverage of TROPOMI over IND is likely responsible for its better performance in constraining methane emissions (see section 4.3.2 for more discussion).
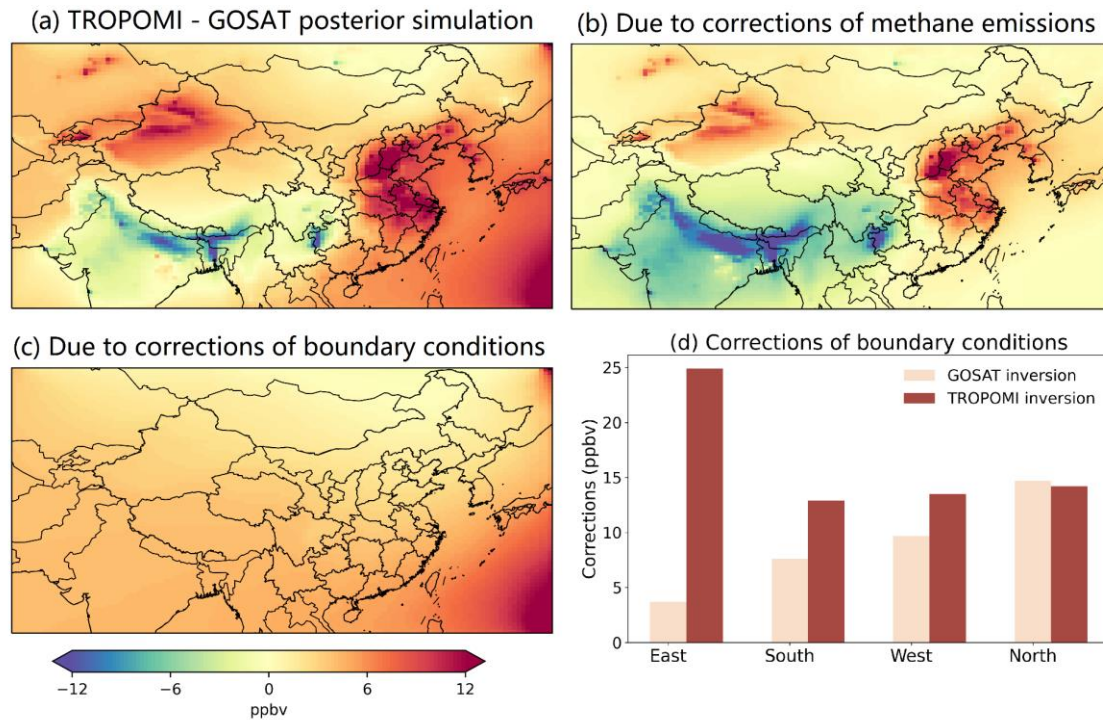
Figure 5: Differences in tropospheric methane concentrations (TROPOMI - GOSAT) between GOSAT and TROPOMI posterior simulations. (a) shows the total differences while (b) and (c) decompose the differences to methane emissions and boundary condition bias corrections. The corrections of boundary conditions (in ppbv) by the two inversions are shown.

4.3 Attribution of TROPOMI and GOSAT inversion differences

4.3.1 Regional retrieval bias

To understand the cause of differences in the inferred methane emissions, we first compare coincident TROPOMI and GOSAT XCH$_4$ retrievals. The comparison is done following Zhang et al. (2010) where a CTM simulation is used as an intercomparison platform to account for differences in prior profiles and vertical sensitivity between TROPOMI and GOSAT retrievals. TROPOMI XCH$_4$ are on average higher than GOSAT XCH$_4$ over EC by ~6 ppbv, SXJC by ~10 ppbv, and NWD by ~10 ppbv (Figure 6b), which lead to higher methane emissions inferred by the TROPOMI inversion over these regions (Figure 3). These differences persist throughout the year in EC and SXJC but appear to be highly seasonal in NWD. The largest TROPOMI-GOSAT differences in NWD (~30-40 ppbv) occur between December and March. In other regions of interest, the annual

averaged TROPOMI-GOSAT XCH4 differences are in general less than 5 ppbv including IND where the two inversions find large discrepancies in posterior methane emissions.

Independent ground-based observations are more consistent with the GOSAT inversion and thus do not support high emissions from EC inferred by the TROPOMI inversion, which indicates that TROPOMI retrievals have systematic regional high biases over EC. In addition, even with enhanced methane emissions in EC, SXJC, and NWD from the TROPOMI inversion, the posterior simulation cannot fully capture these high XCH4 concentrations (Figure 4d). This is also a hint of retrieval biases, as it indicates that the inversion finds it difficult to reconcile these high XCH4 patterns with known methane sources and wind information, given our specification of error parameters ($\mathbf{S_A}$, $\mathbf{S_O}$, and γ).

Figure 6: Differences in XCH4 between GOSAT and TROPOMI (defined as TROPOMI-GOSAT) shown on the 0.5°×0.625° grid (a) and by region (b). (a) shows annual averages for each grid cell and (b) shows time series of regional averages. Regions are defined in blue rectangles of Figure 3a.

In addition to EC, large XCH4 differences between GOSAT and TROPOMI are also found in the northwestern part of the domain (SXJC and NWD). Although we do not have independent observations over these regions, we speculate that TROPOMI retrievals have positive biases. SXJC is featured with high surface albedo (desert), while in NWD large TROPOMI and GOSAT differences occur during Dec and Mar when surface albedo is low (snow and/or ice cover) (Figure S7). High and low surface albedo scenes are known to be challenging for the full-physics retrieval. We suggest to apply the "blended albedo" filter to TROPOMI observations over these regions before inversion (Chen et al., 2022; Wunch et al., 2011).

In our study, we use the TROPOMI science product from Lorente et al. (2021), who applied a posterior correction for surface albedo dependent biases identified in originally retrieved TROPOMI data. We find that this bias correction scheme does overall improve the agreement between TROPOMI and GOSAT in both their methane column concentrations (Figure S8) and posterior methane emissions (Figure S9). However, the agreement is not improved in EC, SXJC, and NWD.

Previous studies have reported decreased accuracy of GOSAT CO_2 proxy retrievals in India owing to errors in the specified CO_2 field (Parker et al., 2015; Schepers et al., 2012). Our result shows that TROPOMI XCH_4 is lower than GOSAT XCH_4 in the western Ganges Plain and higher in a few locations outside the Ganges Plain (Figure 6a), but the regional difference between the two retrievals is overall small (< 5 ppbv) in IND compared to those in EC, SXJC, and NWD (Figure 6b). Exceptions are November and December when the differences are up to 20 ppbv in IND.

4.3.2 Spatial coverage of observations

Although methane emissions from IND (along the Ganges Plain) inferred by the GOSAT inversion are considerably larger than those inferred by the TROPOMI inversion, we find relatively small differences in coincident XCH_4 retrievals there (Figure 6), indicating that retrieval biases are unlikely the only cause of discrepancies. We have shown above that indirect comparison with CARIBIC tropospheric aircraft measurements favors lower emissions from IND estimated by the TROPOMI inversion (Table 1). In this section, we explore whether differences in data coverage between TROPOMI and GOSAT may contribute to the discrepancies in inferred emissions.
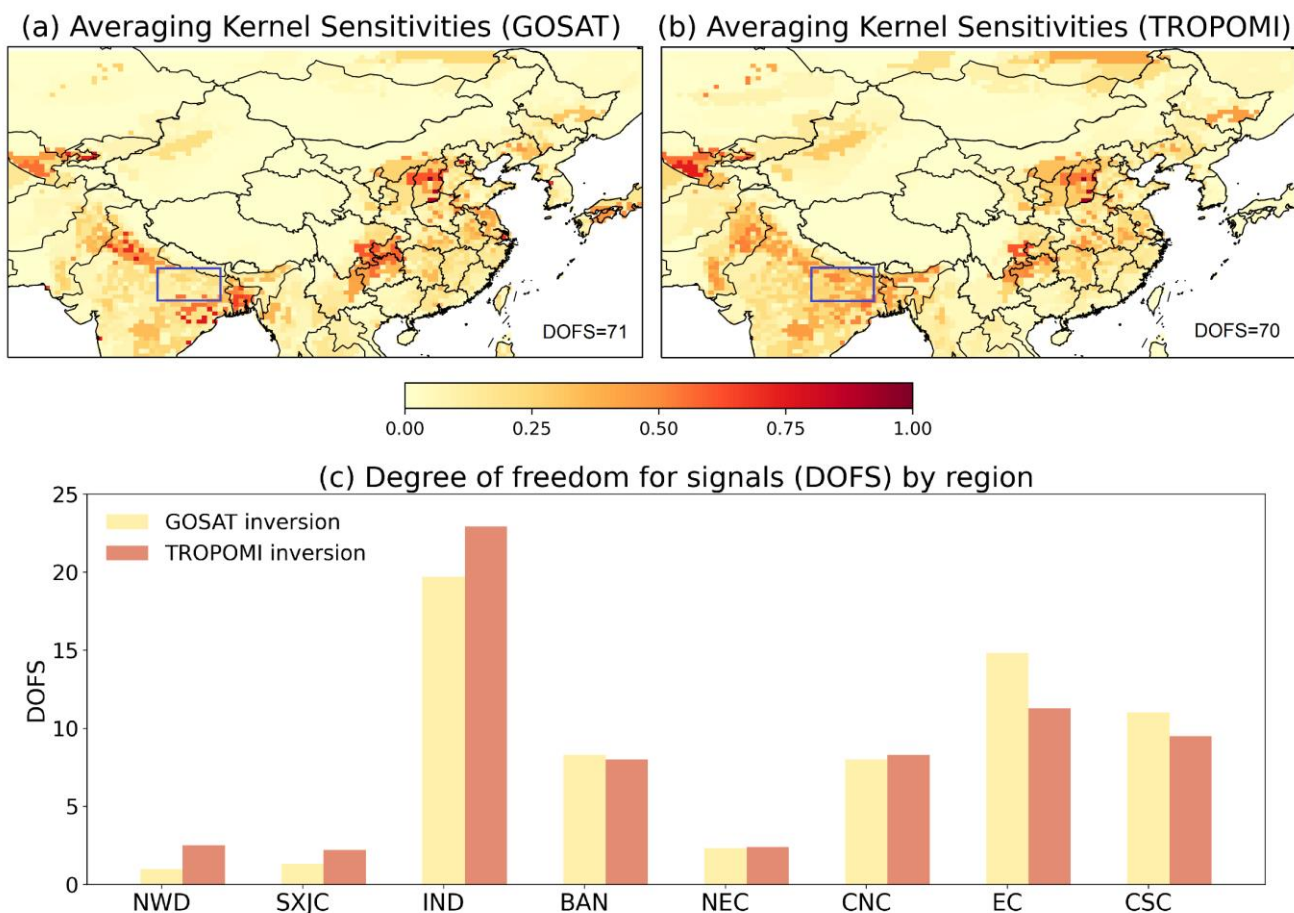
Figure 7: Averaging kernel sensitivities for GOSAT (a) and TROPOMI (b) inversions. Values represent the ability of observations to constrain methane emissions (0 = not at all, 1 = perfectly). The east Ganges Plain is marked by blue rectangles. Panel (c) compares the DOFS of regional emissions constrained by TROPOMI and GOSAT inversions.

Figure 7 compares the ability of TROPOMI and GOSAT inversions to constrain the distribution of methane emissions, measured by averaging kernel sensitivities (diagonal elements of the averaging kernel matrix). This measure accounts for spatial and temporal data coverage, measurement and model errors (through $\mathbf{S_O}$), and error correlations between closely located observations (through γ). The sum of averaging kernel sensitivities over a region represents the number of pieces of independent information (also known as degree of freedom for signals, DOFS) constrained by an observation system. Figure 7c shows that the TROPOMI inversion has a larger DOFS value (23) than does the GOSAT inversion (19) in IND indicating that methane emissions from IND are better resolved by TROPOMI observations. More importantly, the GOSAT inversion results in highly uneven spatial patterns in averaging kernel sensitivities with much lower values found in the east Ganges Plain (corresponding DOFS is 4.5 for GOSAT and 7.4 for TROPOMI; blue rectangles in Figure 7a and 7b) because of a small number of GOSAT observations there (Figure S2) which indicates that the large upward adjustment by the GOSAT inversion

over IND (Figure 3a) is associated with large uncertainties. In contrast, more uniform patterns in averaging kernel sensitivities are achieved by the TROPOMI inversion (Figure 7b).

405

The above analysis demonstrates that the TROPOMI inversion benefits from better data coverage for estimating methane emissions from IND. However, over the entire East Asia domain, TROPOMI and GOSAT achieves almost the same (70) DOFS, with similar spatial patterns of averaging kernel sensitivities (Figure 7). Although the number of TROPOMI observations is much larger, strong error correlations in densely distributed data reduce the efficacy of individual observations, as shown by the difference in the regularization parameter determined for TROPOMI ($\gamma = 0.09$) and GOSAT ($\gamma = 0.6$) observations. Qu et al. (2021) found in coarse-resolution ($2° \times 2.5°$) global inversions that GOSAT achieves ~50% more DOFS than TROPOMI. In our high-resolution regional inversion, TROPOMI achieves relatively higher DOFS which reflects a lower level of error correlation on the $0.5° \times 0.625°$ resolution than $2° \times 2.5°$. It can also be conjectured that TROPOMI observations can provide more information than GOSAT observations in an inversion at a spatial resolution better than $0.5° \times$ 0.625°.

410

415

4.3.3 Regional boundary conditions

Our evaluation against surface observations shows improved agreement at background sites (i.e., PDI, UUM, and WLG) by both inversions (Table 1). This is achieved through simultaneous optimization for biases in boundary conditions together with emissions. As WLG, UUM, and PDI are respectively sensitive to the west, north, and south boundaries, this result suggests that satellite observations can correct biases along these boundaries, supporting our inversion configuration. Furthermore, we find that a sensitivity inversion not optimizing for boundary condition biases (S0) cannot reduce large prior biases at WLG and PDI and leads to unrealistically high methane emissions over East Asia (222 Tg a^{-1}) including China (102 Tg a^{-1}).

420

An exception in Table 1 is LLN (a high-mountain background site in the southeast of the domain) where biases are increased by both inversions. Although the site AMY is also close to the east boundary, it has little influence from the southeast monsoon (Figure 5c). The biases show strong seasonality, with the largest occurring in summer consistent with ocean-to-land (southeast to northwest) transport by summer monsoon. Our analysis suggests that this increase in biases is caused by large adjustments at the east boundary (GOSAT: 3.7 ppbv; TROPOMI: 24.9 ppbv) rather than changes in methane emissions (Figure 5). This result indicates that satellite observations that are mainly over land are insufficient to constrain the east boundary which consists mainly of ocean.

425

430

We then assess the impact of biases along the east boundary on inferred methane emissions. We perform sensitivity inversions using varied levels of fixed (not optimized by the inversion) east boundary conditions, and find relatively small effects on quantifying annual emissions as expected from prevailing westerlies in midlatitudes. A positive bias of 10 ppbv would result in a reduction of annual methane emissions by 2.9 Tg a^{-1} (~2%) over the East Asia domain, 1.6 Tg a^{-1} (~2%) over China, and

435

0.7 Tg a^{-1} (~3%) over EC (the most affected region) (Figure 8). Although the inversion has a weak constraint on the east boundary conditions, it does not have a great influence on the posterior emissions. However, if the inversion is performed on the monthly or seasonal basis (as opposed to annually in this study), summer results will be more severely affected, leading to seasonal biases in inferred methane emissions.
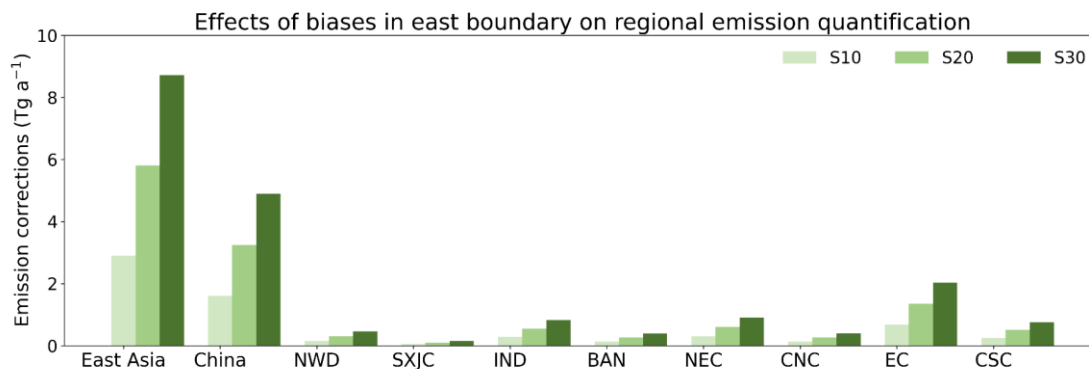
440

Figure 8: Impact of biases in the east boundary on quantification of annual methane emissions. Inversions are performed by using fixed east boundary conditions. Sensitivity results are computed from perturbing these fixed east boundary conditions by 10 (S10), 20 (S20), and 30 (S30) ppbv.

5 Conclusions

445 We estimate methane emissions from East Asia for 2019 by applying atmospheric methane column retrievals from two different satellite instruments (GOSAT and TROPOMI) to a high-resolution regional inversion framework, in which methane emissions are optimized on 600 spatial clusters with up to about half degree horizontal resolution. Our objective is to assess if consistent methane emissions from East Asia are inferred from inversion of GOSAT and TROPOMI observations. This information adds to the uncertainty characterization of satellite-data-based methane emission quantification.

450

The two inversions estimate a similar magnitude of methane emissions from East Asia (TROPOMI: 143.5 Tg a^{-1}; GOSAT: 146.2 Tg a^{-1}) as compared to prior estimate (130 Tg a^{-1}) but differ by ~10% in China (TROPOMI: 74.9 Tg a^{-1}; GOSAT: 68.1 Tg a^{-1}). Comparisons at the regional scale show that the GOSAT and TROPOMI inversions find consistent results over Central North China, Central South China, Northeast China, and Bangladesh, where the inferred emissions differ by less than 2.7 Tg

455 a^{-1}. However, the two inversions show large differences over some of the important regions including northern India and East China. The inferred methane emissions by GOSAT observations are 7.7 Tg a^{-1} higher than those by TROPOMI over northern India but 7.0 Tg a^{-1} lower over East China. Large differences in inferred emissions are also found in northwestern China and Kazakhstan (SXJC and NWD).

460   We evaluate the inversion results by comparing GOSAT and TROPOMI posterior simulations with independent observations. We find that independent ground-based *in situ* observations at AMY and total column observations at XH and HF are more compatible with lower methane emissions from East China inferred by the GOSAT inversion than those by the TROPOMI inversion. We also indirectly evaluate against tropospheric aircraft observations over India during 2012-2014 by using a consistent GOSAT inversion of earlier years as an inter-comparison platform, which favors lower methane emissions from

465   northern India inferred by the TROPOMI inversion over those by the GOSAT inversion.

The fact that high East China emissions inferred from TROPOMI are inconsistent with independent observations suggests high regional biases in TROPOMI retrievals over East China. Large retrieval differences between GOSAT and TROPOMI are also found in the northwestern China and Kazakhstan, which also leads to substantially higher methane emissions inferred by the

470   TROPOMI inversion. Unfortunately, we do not have independent observations to evaluate the results in these two regions. However, we note that large TROPOMI XCH$_4$ variations in Kazakhstan and northern Xinjiang are coincident with seasonal changes in surface albedo, suggesting possibly over-correction of surface albedo dependent biases in TROPOMI retrievals at the regional level.

475   The two inversions show large discrepancies in emissions over northern India along the Ganges Plain, although GOSAT and TROPOMI XCH$_4$ values agree reasonably well. We find that the discrepancy in emissions from norther India is due mainly to differences in data coverage. Analyses of the averaging kernel matrices show that the TROPOMI inversion can better constrain emissions from northern India (especially the eastern part of the Ganges Plain), owing to its good spatial coverage in the region as compared to highly uneven coverage by GOSAT. Over the entire East Asia domain, however, the two inversions show

480   similar ability in constraining the distribution of methane emissions, despite a much larger number of TROPOMI observations. This is due mainly to strong error correlations in dense TROPOMI data at the $0.5° \times 0.625°$ resolution.

Both inversions show improved agreement at background sites supporting our optimization of boundary condition biases. An exception is LLN where both inversions show large positive concentration biases against *in situ* measurements, which results

485   from over-corrections at the eastern boundary by inversions. However, our simulations demonstrate that methane concentration biases at the eastern boundary have relatively small impacts on annual emission inferences. The newer version of the TROPOMI methane product includes glint-mode ocean observations, which may benefit the optimization of eastern boundary conditions.

Data availability

490   The TROPOMI methane observations are from https://ftp.sron.nl/open-access-data-2/TROPOMI/tropomi/ch4/14_14_Lorente_et_al_2020_AMTD (last access: 29 December 2021). The GOSAT methane

observations are the University of Leicester GOSAT Proxy XCH₄ v9.0 (ceda.ac.uk), accessible through https://data.ceda.ac.uk/neodc/gosat/data/ch4/nceov1.0/CH4_GOS_OCPR/, or the Copernicus Climate Data Store (https://cds.climate.copernicus.eu/). Surface observations at PDI are downloaded from https://gaw.kishou.go.jp/. Surface

495 observations at AMY, LLN, UUM, and WLG and aircraft observations from the CARIBIC project are available via the NOAA ObsPack CH₄ product (https://gml.noaa.gov/ccgg/obspack/index.html). The Xianghe FTIR CH₄ data are accessible through https://doi.org/10.18758/71021049. The Hefei FTIR CH₄ from TCCON network can be accessed by contacting Prof. Cheng Liu at University of Science and Technology of China.

Author Contributions

500 RL and YZ designed the study. RL performed the inverse modelling with contributions from YZ, JL, WC, PZ, ZQ, and ZC. RL analysed and interpreted results with contributions from YZ, CC, HM, GS, ZQ, MZ, RJP, HB, AL, JDM, and IA. RJP and HB provided the GOSAT methane retrievals. AL, JDM, and IA provided the TROPOMI methane retrievals. MZ and PW provided ground based FTIR methane retrievals at the Xianghe site. RL and YZ wrote the paper with inputs from all authors.

Acknowledgements

505 This research is supported by the National Key Research and Development Program of China (2021YFB3901000) and the National Natural Science Foundation of China (42007198). We thank the team that realized the TROPOMI instrument and its data products, consisting of the partnership between Airbus Defense and Space Netherlands, KNMI, SRON, and TNO, commissioned by NSO and ESA. Sentinel-5 Precursor is part of the EU Copernicus program, Copernicus (modified) Sentinel-5P data (2018-2020) have been used. Alba Lorente acknowledges funding through the TROPOMI national programme from

510 NSO. We thank the Japanese Aerospace Exploration Agency, National Institute for Environmental Studies, and the Ministry of Environment for the GOSAT data and their continuous support as part of the Joint Research Agreement. Robert J. Parker and Hartmut Boesch acknowledge support from the UK National Centre for Earth Observation funded by the National Environment Research Council (NE/R016518/1 and NE/N018079/1) and the Copernicus Climate Change Service (C3S2_312a_Lot2). The research of GOSAT retrievals used the ALICE High Performance Computing Facility at the

515 University of Leicester. We thank the TCCON community and Weidong Nan (IAP) for supporting the Xianghe FTIR measurements, and the Department of Precision Machinery and Precision Instrumentation, University of Science and Technology of China (Cheng Liu's group) for providing ground-based remote sensing data (Hefei) with their own independent intellectual property rights. We thank Korea Meteorological Administration, Viet Nam Meteorological and Hydrological Administration, China Meteorological Administration, and NOAA for providing surface measurements through

520 GLOBALVIEWplus CH₄ ObsPack and WDCGG. We thank the High-performance Computing Center of Westlake University and National Supercomputing Center at Wuxi for facility support and technical assistance.

References

Alexe, M., Bergamaschi, P., Segers, A. J., Detmers, R., Butz, A., Hasekamp, O. P., Guerlet, S., Parker, R. J., Boesch, H., Frankenberg, C., Scheepmaker, R. A., Dlugokencky, E. J., Sweeney, C., Wofsy, S. C., and Kort, E. A.: Inverse modelling of
525   CH_4 emissions for 2010-2011 using different satellite retrieval products from GOSAT and SCIAMACHY, Atmos. Chem. Phys., 15, 113-133, https://doi.org/10.5194/acp-15-113-2015, 2015.

Bloom, A. A., Bowman, K. W., Lee, M., Turner, A. J., Schroeder, R., Worden, J. R., Weidner, R. J., McDonald, K., and Jacob, D. J.: A global wetland methane emissions and uncertainty dataset for atmospheric chemical transport models (WetCHARTs version 1.0), Geosci. Model Dev., 10, 2141-2156, https://doi.org/10.5194/gmd-10-2141-2017, 2017.

530   Brasseur, G. P. and Jacob, D. J.: Modeling of Atmospheric Chemistry, Cambridge University Press, Cambridge, USA, 2017.

Butz, A., Guerlet, S., Hasekamp, O. P., Schepers, D., Galli, A., Aben, I., Frankenberg, C., Hartmann, J.-M., Tran, H., Kuze, A., KeppeŒ Aleks, G., Toon, G. C., Wunch, D., Wennberg, P. O., Deutscher, N. M., Griffith, D. W. T., Macatangay, R., Messerschmidt, J., Notholt, J., and Warneke, T.: Toward accurate CO_2 and CH_4 observations from GOSAT, Geophys. Res. Lett., 38, L14812, https://doi.org/10.1029/2011GL047888, 2011.

535   Chen, Z., Jacob, D. J., Nesser, H., Sulprizio, M. P., Lorente, A., Varon, D. J., Lu, X., Shen, L., Qu, Z., Penn, E., and Yu, X.: Methane emissions from China: a high-resolution inversion of TROPOMI satellite observations, Atmos. Chem. Phys. Discuss., https://doi.org/10.5194/acp-2022-303, 2022.

Cressot, C., Chevallier, F., Bousquet, P., Crevoisier, C., Dlugokencky, E. J., Fortems-Cheiney, A., Frankenberg, C., Parker, R., Pison, I., Scheepmaker, R. A., Montzka, S. A., Krummel, P. B., Steele, L. P., and Langenfelds, R. L.: On the consistency
540   between global and regional methane emissions inferred from SCIAMACHY, TANSO-FTS, IASI and surface measurements, Atmos. Chem. Phys., 14, 577-592, https://doi.org/10.5194/acp-14-577-2014, 2014.

Deng, Z., Ciais, P., Tzompa-Sosa, Z. A., Saunois, M., Qiu, C., Tan, C., Sun, T., Ke, P., Cui, Y., Tanaka, K., Lin, X., Thompson, R. L., Tian, H., Yao, Y., Huang, Y., Lauerwald, R., Jain, A. K., Xu, X., Bastos, A., Sitch, S., Palmer, P. I., Lauvaux, T., d'Aspremont, A., Giron, C., Benoit, A., Poulter, B., Chang, J., Petrescu, A. M. R., Davis, S. J., Liu, Z., Grassi, G., Albergel,
545   C., Tubiello, F. N., Perugini, L., Peters, W., and Chevallier, F.: Comparing national greenhouse gas budgets reported in UNFCCC inventories against atmospheric inversions, Earth Syst. Sci. Data, 14, 1639-1675, https://doi.org/10.5194/essd-14-1639-2022, 2022.

Dlugokencky, E. J., Steele, L. P., Lang, P. M., and Masarie, K. A.: The growth rate and distribution of atmospheric methane, J. Geophys. Res., 99, 17021-17043, https://doi.org/10.1029/94JD01245, 1994.

550   Dlugokencky, E. J., Nisbet, E. G., Fisher, R. E., and Lowry, D.: Global atmospheric methane: budget, changes and dangers, Philos. Trans. R. Soc. London, Ser. A, 369, 2058 - 2072, https://doi.org/10.1098/rsta.2010.0341, 2011.

Dlugokencky, E. J., Crotwell, A. M., Mund, J. W., Crotwell, M. J., and Thoning, K. W.: Atmospheric Methane Dry Air Mole Fractions from the NOAA GML Carbon Cycle Cooperative Global Air Sampling Network, 1983-2020, Version: 2021-07-30, https://doi.org/10.15138/VNCZ-M766, 2021.

555   Feng, L., Palmer, P. I., Zhu, S., Parker, R. J., and Liu, Y.: Tropical methane emissions explain large fraction of recent changes in global atmospheric methane growth rate, Nature Commun., 13, 1-8, https://doi.org/10.1038/s41467-022-28989-z, 2022.

Fletcher, S. E. M. and Schaefer, H.: Rising methane: A new climate challenge, Science, 364, 932-933, https://doi.org/10.1126/science.aax1828, 2019.

Forster, P., Storelvmo, T., Armour, K., Collins, W., Dufresne, J.-L., Frame, D., Lunt, D. J., Palmer, T. M. M. D., Watanabe, M., Wild, M., and Zhang, H.: The Earth's Energy Budget, Climate Feedbacks, and Climate Sensitivity. In Climate Change 2021: The Physical Science Basis. Contribution of Working Group I to the Sixth Assessment Report of the Intergovernmental Panel on Climate Change, Cambridge University Press, Cambridge, United Kingdom and New York, NY, USA, 2021.

Frankenberg, C., Meirink, J. F., van Weele, M., Platt, U., and Wagner, T.: Assessing Methane Emissions from Global Space-Borne Observations, Science, 308, 1010 - 1014, https://doi.org/10.1071/AN20564, 2005.

Frankenberg, C., Meirink, J. F., Bergamaschi, P., Goede, A. P. H., Heimann, M., Körner, S., Platt, U., Weele, M. v., and Wagner, T.: Satellite chartography of atmospheric methane from SCIAMACHY on board ENVISAT: Analysis of the years 2003 and 2004, J. Geophys. Res., 111, https://doi.org/10.1029/2005JD006235, 2006.

Fung, I. Y., John, J. G., Lerner, J., Matthews, E., Prather, M. J., Steele, L. P., and Fraser, P. J.: Three dimensional model synthesis of the global methane cycle, J. Geophys. Res., 96, 13033-13065, https://doi.org/10.1029/91JD01247, 1991.

Ganesan, A. L., Rigby, M., Lunt, M. F., Parker, R. J., Boesch, H., Goulding, N., Umezawa, T., Zahn, A., Chatterjee, A., Prinn, R. G., Tiwari, Y. K., van der Schoot, M., and Krummel, P. B.: Atmospheric observations show accurate reporting and little growth in India's methane emissions, Nature Commun., 8, 836, https://doi.org/10.1038/s41467-017-00994-7, 2017.

Ganesan, A. L., Schwietzke, S., Poulter, B. I., Arnold, T., Lan, X., Rigby, M. L., Vogel, F. R., Werf, G. R., Janssens-Maenhout, G., Boesch, H., Pandey, S., Manning, A. J., Jackson, R. B., Nisbet, E. G., and Manning, M. R.: Advancing Scientific Understanding of the Global Methane Budget in Support of the Paris Agreement, Global Biogeochem. Cy., 33, 1475 - 1512, https://doi.org/10.1029/2018GB006065, 2019.

Gao, J., Guan, C., Zhang, B., and Li, K.: Decreasing methane emissions from China's coal mining with rebounded coal production, Environ. Res. Lett., 16, https://doi.org/10.1088/1748-9326/ac38d8, 2021.

Gelaro, R., McCarty, W., Suárez, M. J., Todling, R., Molod, A., Takacs, L., Randles, C. A., Darmenov, A. S., Bosilovich, M. G., Reichle, R. H., Wargan, K., Coy, L., Cullather, R. I., Draper, C., Akella, S., Buchard, V., Conaty, A., Silva, A. M. d., Gu, W., Kim, G.-K., Koster, R. D., Lucchesi, R., Merkova, D., Nielsen, J. E., Partyka, G., Pawson, S., Putman, W. M., Rienecker, M. M., Schubert, S., Sienkiewicz, M., and Zhao, B.: The Modern-Era Retrospective Analysis for Research and Applications, Version 2 (MERRA-2), Journal of climate, Volume 30 Iss 13, 5419-5454, https://doi.org/10.1175/jcli-d-16-0758.1, 2017.

Hansen, P. C.: Rank-Deficient and Discrete Ill-Posed Problems: Numerical Aspects of Linear Inversion, Society for Industrial and Applied Mathematics, USA, 1998.

Heald, C. L., Jacob, D. J., Jones, D. B. A., Palmer, P. I., Logan, J. A., Streets, D. G., Sachse, G. W., Gille, J., Hoffman, R. N., and Nehrkorn, T.: Comparative inverse analysis of satellite (MOPITT) and aircraft (TRACE-P) observations to estimate Asian sources of carbon monoxide, J. Geophys. Res., 109, 1-17, https://doi.org/10.1029/2005JD006235, 2004.

Hu, H., Hasekamp, O. P., Butz, A., Galli, A., Landgraf, J., Brugh, J. a. d., Borsdorff, T., Scheepmaker, R. A., and Aben, I.: The operational methane retrieval algorithm for TROPOMI, Atmos. Meas. Tech., 9, 5423-5440, https://doi.org/10.5194/amt-9-5423-2016, 2016.

Hu, H., Landgraf, J., Detmers, R., Borsdorff, T., Brugh, J. a. d., Aben, I., Butz, A., and Hasekamp, O. P.: Toward Global Mapping of Methane With TROPOMI: First Results and Intersatellite Comparison to GOSAT, Geophys. Res. Lett., 45, 3682-3689, https://doi.org/10.1002/2018GL077259, 2018.

595   Jacob, D. J., Turner, A. J., Maasakkers, J. D., Sheng, J., Sun, K., Liu, X., Chance, K. V., Aben, I., Mckeever, J., and Frankenberg, C.: Satellite observations of atmospheric methane and their value for quantifying methane emissions, Atmos. Chem. Phys., 16, 14371-14396, https://doi.org/10.5194/acp-16-14371-2016, 2016.

Jacob, D. J., Varon, D. J., Cusworth, D. H., Dennison, P. E., Frankenberg, C., Gautam, R., Guanter, L., Kelley, J., McKeever, J., Ott, L. E., Poulter, B., Qu, Z., Thorpe, A. K., Worden, J. R., and Duren, R. M.: Quantifying methane emissions from the
600   global scale down to point sources using satellite observations of atmospheric methane, Atmos. Chem. Phys., 22, 9617-9646, 10.5194/acp-22-9617-2022, 2022.

Janssen-Maenhout, G., Crippa, M., Guizzardi, D., Muntean, M., Schaaf, E., Dentener, F. J., Bergamaschi, P., Pagliari, V., Olivier, J. G. J., Peters, J., van Aardenne, J. A., Monni, S., Doering, U., Petrescu, A. M. R., Solazzo, E., and Oreggioni, G. D.: EDGAR v4.3.2 Global Atlas of the three major greenhouse gas emissions for the period 1970-2012, Earth Syst. Sci. Data, 11,
605   959–1002, https://doi.org/10.5194/essd-11-959-2019, 2019.

Kuze, A., Suto, H., Nakajima, M., and Hamazaki, T.: Thermal and near infrared sensor for carbon observation Fourier-transform spectrometer on the Greenhouse Gases Observing Satellite for greenhouse gases monitoring, Applied optics, 48 35, 6716-6733, https://doi.org/10.1364/ao.48.006716, 2009.

Kuze, A., Suto, H., Shiomi, K., Kawakami, S., Tanaka, M., Ueda, Y., Deguchi, A., Yoshida, J., Yamamoto, Y., Kataoka, F.,
610   Taylor, T. E., and Buijs, H.: Update on GOSAT TANSO-FTS performance, operations, and data products after more than 6 years in space, Atmos. Meas. Tech., 9, 2445-2461, https://doi.org/10.5194/amt-9-2445-2016, 2016.

Lee, H., Han, S. O., Ryoo, S. B., Lee, J. S., and Lee, G. W.: The measurement of atmospheric CO_2 at KMA GAW regional stations, its characteristics, and comparisons with other East Asian sites, Atmos. Chem. Phys., 19, 2149-2163, https://doi.org/10.5194/acp-19-2149-2019, 2019.

615   Liu, C., Sun, Y., Shan, C., Wang, W., Notholt, J., Palm, M., Yin, H., Tian, Y., Gao, J., and Mao, H.: Long-term observations of atmospheric constituents at the first ground-based high-resolution fourier-transform spectrometry observation station in china, Engineering, https://doi.org/10.1016/j.eng.2021.11.022, 2022.

Liu, G., Peng, S., Lin, X., Ciais, P., Li, X., Xi, Y., Lu, Z., Chang, J., Saunois, M., Wu, Y., Patra, P. K., Chandra, N., Zeng, H., and Piao, S.: Recent Slowdown of Anthropogenic Methane Emissions in China Driven by Stabilized Coal Production, Environ.
620   Sci. Technol. Lett., https://doi.org/10.1021/acs.estlett.1c00463, 2021.

Lorente, A., Borsdorff, T., Butz, A., Hasekamp, O. P., aan de Brugh, J., Schneider, A., Wu, L., Hase, F., Kivi, R., Wunch, D., Pollard, D. F., Shiomi, K., Deutscher, N. M., Velazco, V. A., Roehl, C. M., Wennberg, P. O., Warneke, T., and Landgraf, J.: Methane retrieved from TROPOMI: improvement of the data product and validation of the first 2 years of measurements, Atmos. Meas. Tech., 14, 665-684, https://doi.org/10.5194/amt-14-665-2021, 2021.

625   Lorente, A., Borsdorff, T., Landgraf, J., and the SRON L2 team: SRON RemoTeC-S5P scientific XCH4 data product Product User Guide, 2022.

Lu, X., Jacob, D. J., Zhang, Y., Maasakkers, J. D., Sulprizio, M. P., Shen, L., Qu, Z., Scarpelli, T. R., Nesser, H., Yantosca, R. M., Sheng, J., Andrews, A. E., Parker, R. J., Boesch, H., Bloom, A. A., and Ma, S.: Global methane budget and trend, 2010-2017: complementarity of inverse analyses using in situ (GLOBALVIEWplus CH_4 ObsPack) and satellite (GOSAT)
630   observations, Atmos. Chem. Phys., 21, 4637-4657, https://doi.org/10.5194/acp-21-4637-2021, 2021.

Maasakkers, J. D., Jacob, D. J., Sulprizio, M. P., Scarpelli, T. R., Nesser, H., Sheng, J., Zhang, Y., Hersher, M., Bloom, A. A., Bowman, K. W., Worden, J. R., Janssens Maenhout, G., and Parker, R. J.: Global distribution of methane emissions, emission

trends, and OH concentrations and trends inferred from an inversion of GOSAT satellite data for 2010-2015, Atmos. Chem. Phys., 19, 7859–7881, https://doi.org/10.5194/acp-19-7859-2019, 2019.

635 McNorton, J., Bousserez, N., Agustí-Panareda, A., Balsamo, G., Cantarello, L., Engelen, R., Huijnen, V., Inness, A., Kipling, Z., Parrington, M., and Ribas, R.: Quantification of methane emissions from hotspots and during COVID-19 using a global atmospheric inversion, Atmos. Chem. Phys., 22, 5961-5981, https://doi.org/10.5194/acp-22-5961-2022, 2022.

Miller, S. M., Michalak, A. M., Detmers, R., Hasekamp, O. P., Bruhwiler, L., and Schwietzke, S.: China's coal mine methane regulations have not curbed growing emissions, Nature Commun., 10, https://doi.org/10.1038/s41467-018-07891-7, 2019.

640 Monteil, G., Houweling, S., Butz, A., Guerlet, S., Schepers, D., Hasekamp, O. P., Frankenberg, C., Scheepmaker, R. A., Aben, I., and Röckmann, T.: Comparison of CH_4 inversions based on 15 months of GOSAT and SCIAMACHY observations, J. Geophys. Res. Atmos., 118, 11807-11823, https://doi.org/10.1002/2013JD019760, 2013.

Murguia-Flores, F., Arndt, S., Ganesan, A. L., Murray-Tortarolo, G. N., and Hornibrook, E. R. C.: Soil Methanotrophy Model (MeMo v1.0): a process-based model to quantify global uptake of atmospheric methane by soil, Geosci. Model Dev., 11, 2009–
645 2032, https://doi.org/10.5194/gmd-11-2009-2018, 2018.

Nguyen Nhat Anh and Steinbacher, M.: Atmospheric CH_4 at Pha Din by Viet Nam Meteorological and Hydrological Administration , dataset published as CH4_PDI_surface-insitu_VNMHA_data1 at WDCGG, ver. 2020-07-13-2137, https://doi.org/10.50849/WDCGG_0051-2035-1002-01-01-9999, 2021.

Nisbet, E. G., Manning, M. R., Dlugokencky, E. J., Fisher, R. E., Lowry, D., Michel, S. E., Myhre, C. L., Platt, S. M., Allen,
650 G., Bousquet, P., Brownlow, R., Cain, M., France, J. L., Hermansen, O., Hossaini, R., Jones, A. E., Levin, I., Manning, A. C., Myhre, G., Pyle, J. A., Vaughn, B. H., Warwick, N. J., and White, J. W. C.: Very Strong Atmospheric Methane Growth in the 4 Years 2014–2017: Implications for the Paris Agreement, Global Biogeochem. Cy., 33, 318-342, https://doi.org/10.1029/2018GB006009, 2019.

Pandey, S., Houweling, S., Krol, M. C., Aben, I., Chevallier, F., Dlugokencky, E. J., Gatti, L. V., Gloor, E., Miller, J. B.,
655 Detmers, R., Machida, T., and Röckmann, T.: Inverse modeling of GOSAT-retrieved ratios of total column CH_4 and CO_2 for 2009 and 2010, Atmos. Chem. Phys., 16, 5043-5062, https://doi.org/10.5194/acp-16-5043-2016, 2016.

Parker, R. J., Boesch, H., Byckling, K., Webb, A. J., Palmer, P. I., Feng, L., Bergamaschi, P., Chevallier, F., Notholt, J., Deutscher, N., Warneke, T., Hase, F., Sussmann, R., Kawakami, S., Kivi, R., Griffith, D. W. T., and Velazco, V.: Assessing 5 years of GOSAT Proxy XCH_4 data and associated uncertainties, Atmos. Meas. Tech., 8, 4785-4801,
660 https://doi.org/10.5194/amt-8-4785-2015, 2015.

Parker, R. J. and Boesch, H.: University of Leicester GOSAT Proxy XCH_4 v9.0. Centre for Environmental Data Analysis, http://dx.doi.org/10.5285/18ef8247f52a4cb6a14013f8235cc1eb, 2020.

Parker, R. J., Webb, A., Boesch, H., Somkuti, P., Barrio Guillo, R., Di Noia, A., Kalaitzi, N., Anand, J. S., Bergamaschi, P., Chevallier, F., Palmer, P. I., Feng, L., Deutscher, N. M., Feist, D. G., Griffith, D. W. T., Hase, F., Kivi, R., Morino, I., Notholt,
665 J., Oh, Y. S., Ohyama, H., Petri, C., Pollard, D. F., Roehl, C., Sha, M. K., Shiomi, K., Strong, K., Sussmann, R., Té, Y., Velazco, V. A., Warneke, T., Wennberg, P. O., and Wunch, D.: A decade of GOSAT Proxy satellite CH_4 observations, Earth Syst. Sci. Data, 12, 3383-3412, https://doi.org/10.5194/essd-12-3383-2020, 2020.

Qu, Z., Jacob, D. J., Shen, L., Lu, X., Zhang, Y., Scarpelli, T. R., Nesser, H., Sulprizio, M. P., Maasakkers, J. D., Bloom, A. A., Worden, J. R., Parker, R. J., and Delgado, A. L.: Global distribution of methane emissions: a comparative inverse analysis
670 of observations from the TROPOMI and GOSAT satellite instruments, Atmos. Chem. Phys., 21, 14159-14175, https://doi.org/10.5194/acp-21-14159-2021, 2021.

Rigby, M. L., Prinn, R. G., Fraser, P. J., Simmonds, P. G., Langenfelds, R. L., Huang, J., Cunnold, D. M., Steele, L. P., Krummel, P. B., Weiss, R. F., O'Doherty, S. J., Salameh, P. K., Wang, H. J., Harth, C. M., Mühle, J., and Porter, L. W.: Renewed growth of atmospheric methane, Geophys. Res. Lett., 35, https://doi.org/10.1029/2008GL036037, 2008.

675   Rodgers, C. D.: Inverse Methods for Atmospheric Sounding: Theory and Practice, World Scientific, USA, 2000.

Saunois, M., Stavert, A. R., Poulter, B. I., Bousquet, P., Canadell, J. G., Jackson, R. B., Raymond, P. A., Dlugokencky, E. J., Houweling, S., Patra, P. K., Ciais, P., Arora, V. K., Bastviken, D., Bergamaschi, P., Blake, D. R., Brailsford, G. W., Bruhwiler, L., Carlson, K. M., Carrol, M., Castaldi, S., Chandra, N., Crevoisier, C., Crill, P. M., Covey, K. R., Curry, C. L., Etiope, G., Frankenberg, C., Gedney, N., Hegglin, M. I., Höglund-Isaksson, L., Hugelius, G., Ishizawa, M., Ito, A., Janssen" Maenhout, 680   G., Jensen, K. M., Joos, F., Kleinen, T., Krummel, P. B., Langenfelds, R. L., Laruelle, G. G., Liu, L., Machida, T., Maksyutov, S., McDonald, K., McNorton, J., Miller, P. A., Melton, J. R., Morino, I., Müller, J., Murguia-Flores, F., Naik, V., Niwa, Y., Noce, S., O'Doherty, S. J., Parker, R. J., Peng, C., Peng, S., Peters, G. P., Prigent, C., Prinn, R. G., Ramonet, M., Régnier, P., Riley, W. J., Rosentreter, J. A., Segers, A. J., Simpson, I. J., Shi, H., Smith, S. J., Steele, L. P., Thornton, B. F., Tian, H., Tohjima, Y., Tubiello, F. N., Tsuruta, A., Viovy, N., Voulgarakis, A., Weber, T., van Weele, M., van der Werf, G. R., Weiss, 685   R. F., Worthy, D. E. J., Wunch, D., Yin, Y., Yoshida, Y., Zhang, W., Zhang, Z., Zhao, Y., Zheng, B., Zhu, Q., Zhu, Q., and Zhuang, Q.: The Global Methane Budget 2000-2017, Earth Syst. Sci. Data, 12, 1561-1623, https://doi.org/10.5194/essd-12-1561-2020, 2020.

Scarpelli, T. R., Jacob, D. J., Maasakkers, J. D., Sulprizio, M. P., Sheng, J., Rose, K. K., Romeo, L., Worden, J. R., and Janssen-Maenhout, G.: A global gridded (0.1° x 0.1°) inventory of methane emissions from oil, gas, and coal exploitation based on 690   national reports to the United Nations Framework Convention on Climate Change, Earth Syst. Sci. Data, 12, 563-575, https://doi.org/10.5194/essd-12-563-2020, 2020.

Schepers, D., Guerlet, S., Butz, A., Landgraf, J., Frankenberg, C., Hasekamp, O., Blavier, J.-F., Deutscher, N. M., Griffith, D. W. T., Hase, F., Kyro, E., Morino, I., Sherlock, V., Sussmann, R., and Aben, I.: Methane retrievals from Greenhouse Gases Observing Satellite (GOSAT) shortwave infrared measurements: Performance comparison of proxy and physics retrieval 695   algorithms, J. Geophys. Res. Atmos., 117, https://doi.org/10.1029/2012JD017549, 2012.

Schneising, O., Buchwitz, M., Reuter, M., Bovensmann, H., Burrows, J. P., Borsdorff, T., Deutscher, N. M., Feist, D. G., Griffith, D. W. T., Hase, F., Hermans, C., Iraci, L. T., Kivi, R., Landgraf, J., Morino, I., Notholt, J., Petri, C., Pollard, D. F., Roche, S., Shiomi, K., Strong, K., Sussmann, R., Velazco, V. A., Warneke, T., and Wunch, D.: A scientific algorithm to simultaneously retrieve carbon monoxide and methane from TROPOMI onboard Sentinel-5 Precursor, Atmos. Meas. Tech., 700   12, 6771-6802, 2019.

Schuldt, K. N., Aalto, T., Andrews, A., Aoki, S., Arduini, J., Baier, B., Bergamaschi, P., Biermann, T., Biraud, S. C., Boenisch, H., Brailsford, G., Chen, H., and Colomb, A.: Multi-laboratory compilation of atmospheric methane data for the period 1983-2020; obspack_ch4_1_GLOBALVIEWplus_v4.0_2021-10-14, https://doi.org/10.25925/20211001, 2021.

Sha, M. K., Langerock, B., Blavier, J. F. L., Blumenstock, T., Borsdorff, T., Buschmann, M., Dehn, A., De Mazière, M., 705   Deutscher, N. M., Feist, D. G., García, O. E., Griffith, D. W. T., Grutter, M., Hannigan, J. W., Hase, F., Heikkinen, P., Hermans, C., Iraci, L. T., Jeseck, P., Jones, N., Kivi, R., Kumps, N., Landgraf, J., Lorente, A., Mahieu, E., Makarova, M. V., Mellqvist, J., Metzger, J. M., Morino, I., Nagahama, T., Notholt, J., Ohyama, H., Ortega, I., Palm, M., Petri, C., Pollard, D. F., Rettinger, M., Robinson, J., Roche, S., Roehl, C. M., Röhling, A. N., Rousogenous, C., Schneider, M., Shiomi, K., Smale, D., Stremme, W., Strong, K., Sussmann, R., Té, Y., Uchino, O., Velazco, V. A., Vigouroux, C., Vrekoussis, M., Wang, P., Warneke, T., 710   Wizenberg, T., Wunch, D., Yamanouchi, S., Yang, Y., and Zhou, M.: Validation of methane and carbon monoxide from Sentinel-5 Precursor using TCCON and NDACC-IRWG stations, Atmos. Meas. Tech., 14, 6249-6304, https://doi.org/10.5194/amt-14-6249-202110.5194/amt-14-6249-2021, 2021.

Shen, L., Zavala-Araiza, D., Gautam, R., Omara, M., Scarpelli, T. R., Sheng, J., Sulprizio, M. P., Zhuang, J., Zhang, Y., Qu, Z., Lu, X., Hamburg, S. P., and Jacob, D. J.: Unravelling a large methane emission discrepancy in Mexico using satellite observations, Remote Sens. Environ., 260, https://doi.org/10.1016/j.rse.2021.112461, 2021.

Shen, L., Gautam, R., Omara, M., Zavala-Araiza, D., Maasakkers, J. D., Scarpelli, T. R., Lorente, A., Lyon, D. R., Sheng, J., Varon, D. J., Nesser, H., Qu, Z., Lu, X., Sulprizio, M. P., Hamburg, S. P., and Jacob, D. J.: Satellite quantification of oil and natural gas methane emissions in the US and Canada including contributions from individual basins, Atmos. Chem. Phys. Discuss., https://doi.org/10.5194/acp-2022-155, 2022.

Sheng, J., Song, S., Zhang, Y., Prinn, R. G., and Janssens-Maenhout, G.: Bottom-Up Estimates of Coal Mine Methane Emissions in China: A Gridded Inventory, Emission Factors, and Trends, Environ. Sci. Technol. Lett., 6, 473-478, https://doi.org/10.1021/acs.estlett.9b00294, 2019.

Sheng, J., Tunnicliffe, R. L., Ganesan, A. L., Maasakkers, J. D., Shen, L., Prinn, R. G., Song, S., Zhang, Y., Scarpelli, T. R., Anthony Bloom, A., Rigby, M. L., Manning, A. J., Parker, R. J., Boesch, H., Lan, X., Zhang, B., Zhuang, M., and Lu, X.: Sustained methane emissions from China after 2012 despite declining coal production and rice-cultivated area, Environ. Res. Lett., 16, https://doi.org/10.1088/1748-9326/ac24d1, 2021.

Stavert, A. R., Saunois, M., Canadell, J. G., Poulter, B., Jackson, R. B., Regnier, P., Lauerwald, R., Raymond, P. A., Allen, G. H., Patra, P. K., Bergamaschi, P., Bousquet, P., Chandra, N., Ciais, P., Gustafson, A., Ishizawa, M., Ito, A., Kleinen, T., Maksyutov, S., McNorton, J., Melton, J. R., Müller, J., Niwa, Y., Peng, S., Riley, W. J., Segers, A., Tian, H., Tsuruta, A., Yin, Y., Zhang, Z., Zheng, B., and Zhuang, Q.: Regional trends and drivers of the global methane budget, Global Change Biology, 28, 182-200, https://doi.org/10.1111/gcb.15901, 2022.

Turner, A. J. and Jacob, D. J.: Balancing aggregation and smoothing errors in inverse models, Atmos. Chem. Phys., 15, 7039-7048, https://doi.org/10.5194/acp-15-7039-2015, 2015.

Turner, A. J., Jacob, D. J., Wecht, K. J., Maasakkers, J. D., Lundgren, E. W., Andrews, A. E., Biraud, S. C., Boesch, H., Bowman, K. W., Deutscher, N. M., Dubey, M. K., Griffith, D. W. T., Hase, F., Kuze, A., Notholt, J., Ohyama, H., Parker, R. J., Payne, V. H., Sussmann, R., Sweeney, C., Velazco, V. A., Warneke, T., Wennberg, P. O., and Wunch, D.: Estimating global and North American methane emissions with high spatial resolution using GOSAT satellite data, Atmos. Chem. Phys., 15, 7049-7069, https://doi.org/10.5194/acp-15-7049-2015, 2015.

United Nations Framework Convention on Climate Change: Greenhouse Gas Inventory Data: https://di.unfccc.int/detailed_data_by_party, last access: 30 May 2022.

Veefkind, J. P., Aben, I., McMullan, K., Förster, H., de Vries, J., Otter, G., Claas, J., Eskes, H. J., de Haan, J. F., Kleipool, Q., van Weele, M., Hasekamp, O., Hoogeveen, R., Landgraf, J., Snel, R., Tol, P., Ingmann, P., Voors, R., Kruizinga, B., Vink, R., Visser, H., and Levelt, P. F.: TROPOMI on the ESA Sentinel-5 Precursor: A GMES mission for global observations of the atmospheric composition for climate, air quality and ozone layer applications, Remote Sens. Environ., 120, 70-83, https://doi.org/10.1016/j.rse.2011.09.027, 2012.

Wang, F., Maksyutov, S., Janardanan, R., Tsuruta, A., Ito, A., Morino, I., Yoshida, Y., Tohjima, Y., Kaiser, J. W., Janssens-Maenhout, G., Lan, X., Mammarella, I., Lavric, J. V., and Matsunaga, T.: Interannual variability on methane emissions in monsoon Asia derived from GOSAT and surface observations, Environ. Res. Lett., 16, 024040, http://dx.doi.org/10.1088/1748-9326/abd352, 2021.

Wecht, K. J., Jacob, D. J., Frankenberg, C., Jiang, Z., and Blake, D. R.: Mapping of North American methane emissions with high spatial resolution by inversion of SCIAMACHY satellite data, J. Geophys. Res. Atmos., 119, 7741-7756, https://doi.org/10.1002/2014JD021551, 2014.

WMO: WMO Greenhouse Gas Bulletin - The State of Greenhouse Gases in the Atmosphere Based on Global Observations through 2020, 6-7, 2021.

755   Wunch, D., Wennberg, P. O., Toon, G. C., Connor, B. J., Fisher, B. M., Osterman, G., Frankenberg, C., Mandrake, L., o Dell, C. W., Ahonen, P., Biraud, S. C., Castaño, R., Cressie, N., Crisp, D., Deutscher, N. M., Eldering, A., Fisher, M. L., Griffith, D. W. T., Gunson, M. R., Heikkinen, P., Keppel Aleks, G., Kyrö, E., Lindenmaier, R., Macatangay, R., Mendonca, J., Messerschmidt, J., Miller, C. E., Morino, I., Notholt, J., Oyafuso, F. A., Rettinger, M., Robinson, J., Roehl, C. M., Salawitch, R. J., Sherlock, V., Strong, K., Sussmann, R., Tanaka, T., Thompson, D. R., Uchino, O., Warneke, T., and Wofsy, S. C.: A
760   method for evaluating bias in global measurements of CO_2 total columns from space, Atmos. Chem. Phys., 11, 12317-12337, https://doi.org/10.5194/acp-11-12317-2011, 2011.

Yang, Y., Zhou, M., Langerock, B., Sha, M. K., Hermans, C., Wang, T., Ji, D., Vigouroux, C., Kumps, N., Wang, G., De Mazière, M., and Wang, P.: New ground-based Fourier-transform near-infrared solar absorption measurements of XCO_2, XCH_4 and XCO at Xianghe, China, Earth Syst. Sci. Data, 12, 1679-1696, https://doi.org/10.5194/essd-12-1679-2020, 2020.

765   Yin, Y., Chevallier, F., Ciais, P., Bousquet, P., Saunois, M., Zheng, B., Worden, J., Bloom, A. A., Parker, R. J., Jacob, D. J., Dlugokencky, E. J., and Frankenberg, C.: Accelerating methane growth rate from 2010 to 2017: leading contributions from the tropics and East Asia, Atmos. Chem. Phys., 21, 12631-12647, https://doi.org/10.5194/acp-21-12631-2021, 2021.

Yokota, T., Yoshida, Y., Eguchi, N., Ota, Y., Tanaka, T., Watanabe, H., and Maksyutov, S.: Global Concentrations of CO_2 and CH_4 Retrieved from GOSAT: First Preliminary Results, Sola, 5, 160-163, https://doi.org/10.2151/sola.2009-041, 2009.

770   Yoshida, Y., Kikuchi, N., Morino, I., Uchino, O., Oshchepkov, S., Bril, A., Saeki, T., Schutgens, N., Toon, G. C., Wunch, D., Roehl, C. M., Wennberg, P. O., Griffith, D. W. T., Deutscher, N. M., Warneke, T., Notholt, J., Robinson, J., Sherlock, V., Connor, B., Rettinger, M., Sussmann, R., Ahonen, P., Heikkinen, P., Kyrö, E., Mendonca, J., Strong, K., Hase, F., Dohe, S., and Yokota, T.: Improvement of the retrieval algorithm for GOSAT SWIR XCO_2 and XCH_4 and their validation using TCCON data, Atmos. Meas. Tech., 6, 1533-1547, 10.5194/amt-6-1533-2013, 2013.

775   Zhang, L., Jacob, D. J., Liu, X., Logan, J. A., Chance, K. V., Eldering, A., and Bojkov, B. R.: Intercomparison methods for satellite measurements of atmospheric composition: application to tropospheric ozone from TES and OMI, Atmos. Chem. Phys., 10, 4725-4739, https://doi.org/10.5194/acp-10-4725-2010, 2010.

Zhang, Y., Gautam, R., Pandey, S., Omara, M., Maasakkers, J. D., Sadavarte, P., Lyon, D. R., Nesser, H., Sulprizio, M. P., Varon, D. J., Zhang, R., Houweling, S., Zavala-Araiza, D., Alvarez, R. A., Lorente, A., Hamburg, S. P., Aben, I., and Jacob,
780   D. J.: Quantifying methane emissions from the largest oil-producing basin in the United States from space, Science Advances, 6, https://doi.org/10.1126/sciadv.aaz5120, 2020.

Zhang, Y., Jacob, D. J., Lu, X., Maasakkers, J. D., Scarpelli, T. R., Sheng, J., Shen, L., Qu, Z., Sulprizio, M. P., Chang, J., Bloom, A. A., Ma, S., Worden, J. R., Parker, R. J., and Boesch, H.: Attribution of the accelerating increase in atmospheric methane during 2010-2018 by inverse analysis of GOSAT observations, Atmos. Chem. Phys., 21, 3643-3666,
785   https://doi.org/10.5194/acp-21-3643-2021, 2021.

Zhang, Y., Fang, S., Chen, J., Lin, Y., Chen, Y., Liang, R., Jiang, K., Parker, R. J., Boesch, H., Steinbacher, M., Sheng, J.-X., Lu, X., Song, S., and Peng, S.: Observed changes in China's methane emissions linked to policy drivers, Proceedings of the National Academy of Sciences, 119, e2202742119, https://www.doi.org/10.1073/pnas.2202742119, 2022.